

Laboratory disruption of scaled astrophysical outflows by a misaligned magnetic field

G. Revet,^{1,2,3} B. Khair,^{4,5} E. Filippov,^{6,1} C. Argiroffi,^{7,8} J. Béard,⁹ R. Bonito,⁸ M. Cerchez,¹⁰ S. N. Chen,^{1,11} T. Gangolf,^{10,2} D. P. Higginson,^{2,12} A. Mignone,¹³ B. Olmi,¹⁴ M. Ouillé,² S. N. Ryazantsev,^{6,15} I. Yu. Skobelev,^{6,16} M. I. Safronova,¹ M. Starodubtsev,¹ T. Vinci,² O. Willi,¹⁰ S. Pikuz,^{6,16} S. Orlando,⁸ A. Ciardi,⁴ and J. Fuchs^{1,2}

¹*Institute of Applied Physics, 46 Ulyanov Street, 603950 Nizhny Novgorod, Russia*

²*LULI, CNRS, CEA, Sorbonne Université, École Polytechnique, Institut Polytechnique de Paris, F-91128 Palaiseau, France*

³*Centre Laser Intenses et Applications, Université de Bordeaux-CNRS-CEA, UMR 5107, 33405 Talence, France*

⁴*Sorbonne Université, Observatoire de Paris, PSL Research University, LERMA, CNRS UMR 8112, F-75005, Paris, France*

⁵*Flash Center for Computational Science, University of Chicago, 5640 S. Ellis Avenue, Chicago, IL 60637, USA*

⁶*Joint Institute for High Temperatures, RAS, 125412, Moscow, Russia*

⁷*Dipartimento di Fisica e Chimica, Università di Palermo, Palermo, Italy*

⁸*INAF-Osservatorio Astronomico di Palermo, Palermo, Italy*

⁹*LNCMI, UPR 3228, CNRS-UGA-UPS-INSA, 31400 Toulouse, France*

¹⁰*Institut für Laser und Plasmaphysik, Heinrich Heine Universität Düsseldorf, D-40225 Düsseldorf, Germany*

¹¹*ELI-NP, "Horia Hulubei" National Institute for Physics and Nuclear Engineering, 30 Reactorului Street, RO-077125, Bucharest-Magurele, Romania*

¹²*Lawrence Livermore National Laboratory, Livermore, California 94550, USA*

¹³*Dip. di Fisica, Università di Torino via Pietro Giuria 1 (10125) Torino, Italy*

¹⁴*INAF-Osservatorio Astrofisico di Arcetri, Firenze, Italy*

¹⁵*M. V. Lomonosov Moscow State University, Moscow 119991, Russia*

¹⁶*National Research Nuclear University 'MEPhI', 115409 Moscow, Russia*

The shaping of astrophysical outflows into bright, dense and collimated jets due to magnetic pressure is here investigated using laboratory experiments. We notably look at the impact on jet collimation of a misalignment between the outflow, as it stems from the source, and the magnetic field. For small misalignments, a magnetic nozzle forms and redirects the outflow in a collimated jet. For growing misalignments, this nozzle becomes increasingly asymmetric, disrupting jet formation. Our results thus suggest outflow/magnetic field misalignment to be a plausible key process regulating jet collimation in a variety of objects. Furthermore, they provide a possible interpretation for the observed structuring of astrophysical jets. Jet modulation could be interpreted as the signature of changes over time in the outflow/ambient field angle, and the change in the direction of the jet could be the signature of changes in the direction of the ambient field.

INTRODUCTION

Outflows of matter are general features stemming from accreting objects as varied as black holes, active galactic nuclei (AGNs), pulsar wind nebulae (PWNe), or Young Stellar Objects (YSO). In all these objects, varied morphologies are observed for the outflows, from very high aspect ratio, collimated jets, to short ones that seemingly cannot sustain a high density over a long range. The mechanisms underlying these varied morphologies are however still unclear. What we will present here, and discuss in the light of observations made onto a variety of astrophysical objects, is a possible scenario where the relative orientation between the outflow and the large-scale ambient magnetic field surrounding the object can play a major role orienting the dynamics of the outflow from a collimated one to a stunted one.

Clarifying the question of the dynamics leading to varied outflow morphologies is not limited to answering that sole question, but has also implications in helping understand the global dynamics of the source objects, since the outflows generation is intrinsically connected to the global dynamics of the objects. In YSO, for instance,

the understanding of the outflow dynamics is crucial in acquiring a complete picture of the first stages of star formation. Indeed, it is only through the removal of angular momentum from the system, as provided by the outflow [1–3], that matter can be accreted on the star [4]. YSO jets are supersonically ejected into the ambient medium and often show a well collimated chain of knots detected in several bands, e.g. optical and X-ray bands [5]. YSO jets are detected during the early stages of evolution (class 0 and class I) and in Classical T Tauri Stars, when accretion of material onto the central object is still at work, while are not observed in more evolved stages when the accretion process is no longer active. YSOs outflow genesis is widely accepted, and originates from magneto-centrifugally accelerated disk or stellar winds [3, 4, 6]; the collimation process leading in some cases to remarkably narrow and stable jets [7] is however more controversial.

Bow-shock PWNe are another example of astrophysical sources where collimated jets can be observed. These nebulae are produced by fast moving pulsars (with velocities from hundreds to thousands of km s^{-1}) escaped from their parent supernova remnants [8, 9]. Due to the su-

personic motion of the pulsar, bow-shock PWNe show a cometary-like morphology with the pulsar located at the bright head of the nebula, and the long tail extending in the direction opposite to the pulsar motion (eventually for few pc [9]). Puzzling bright X-ray jets, largely misaligned with the pulsar direction of motion, have been observed in some bow-shock PWNe in the last years [10–14]. Their formation was recently clarified as the result of particles escaping the bow shock at magnetic reconnection locations with the interstellar magnetic field, developing at the magnetopause layer depending on the mutual inclination between the internal and outer fields [15]. Once escaped, particles then illuminate the structure of the ambient magnetic field [13, 16, 17]. However, the directionality of the jets, as well as the distortions that can be observed to affect some of them at certain distances from the pulsar, still remain to be clarified.

Several scenarios have been evoked to explain jet collimation. One of them is the collimation by a toroidal magnetic field (magneto-hydrodynamic self-collimation); however, a dominant toroidal field, i.e. wound-up around the outflow, can potentially drive the jet unstable, as shown, for instance, in numerical simulations of YSO [18], and scaled laboratory experiments [19]. The collimation by a dominant poloidal magnetic field component, i.e. aligned with the outflow, through the pressure exerted by the magnetic field surrounding the outflow, is another plausible scenario [20–23]. This configuration has been recently shown in the laboratory to be very effective in producing long-range, stable and dense jets [24, 25]. The laboratory test of this collimation mechanism has been performed with the outflow axis being aligned with that of the magnetic field. However, this alignment is not expected to be the rule for every astrophysical system. For instance in the magnetically regulated star formation, the outflow is expected to be aligned with the rotation axis of the protostar-disk system but not necessarily with that of the larger scale ~ 50 AU, non-local magnetic field surrounding the system [26]. Moreover, a misalignment of the large-scale magnetic field with the core rotation axis could even be necessary to aid the disk/protostar formation process [27–29]. The reason for this is that, in misaligned configurations, the magnetic braking during the cloud collapse is less efficient, and thus helping the formation of more massive disks (early in the star formation). Also in the case of bow-shock PWNe there is some evidence for a direct impact of the geometry of the ambient magnetic field on the morphology of the system [15].

Regarding this alignment, several observations of YSO have reported, at different length scales, the correlation between the axis of the outflows and that of the surrounding magnetic field [27–29]. Looking at the degree of collimation of the outflows, Strom et al. [30] and Ménard & Duchêne [31] highlight the preferential alignment of well collimated, bright, long-range jets with the magnetic

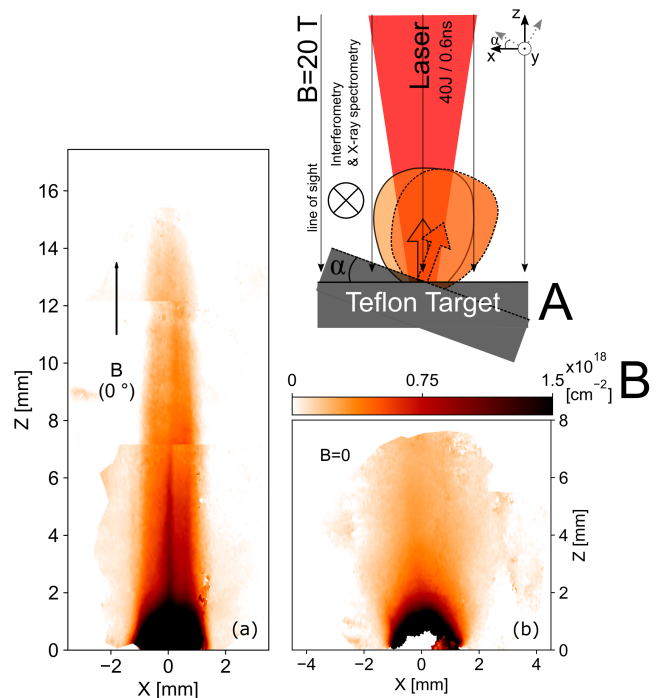


FIG. 1. **Schematic of experimental set-up and observed plasma expansion, with and without an aligned magnetic field.** **A:** Sketch of the experimental setup. The target is embedded in a large-scale 20 T magnetic field, and is heated by a $I_{max} = 1.6 \times 10^{13} \text{ W cm}^{-2}$, 0.6 ns duration laser. By tilting the target, it is possible to vary the angle α between the main plasma outflow direction and that of the magnetic field. The plasma is optically probed along the y axis. **B:** (a) Laboratory maps of the electron density integrated along the probe line of sight, in $[\text{cm}^{-2}]$, retrieved via interferometric measurement (see Methods), at **28 ns** after the start of the plasma expansion. The vertical black arrows indicate the magnetic field direction; here aligned with the main axis of plasma expansion (i.e. along z; $z = 0$ being the target surface). (b) Same without any magnetic field applied. In both panels, the contour follows the $2 \times 10^{17} \text{ cm}^{-2}$ integrated density value.

field, while weaker or wider jets oppositely present a preferential misalignment.

RESULTS

Here we report on a laboratory experiment in which a wide angle expanding plasma outflow, generated by ablating plasma from a solid by a high-power laser, is interacting with a large-scale magnetic field, homogeneous and permanent at the scales of the experiment, having a variable orientation with respect to the outflow main axis. As detailed in the Methods section and Table I (see also Refs. [24, 25]), such setup is shown to be scalable to a YSO wide angle outflow interacting with an ambient magnetic field within the 10 to 50 AU

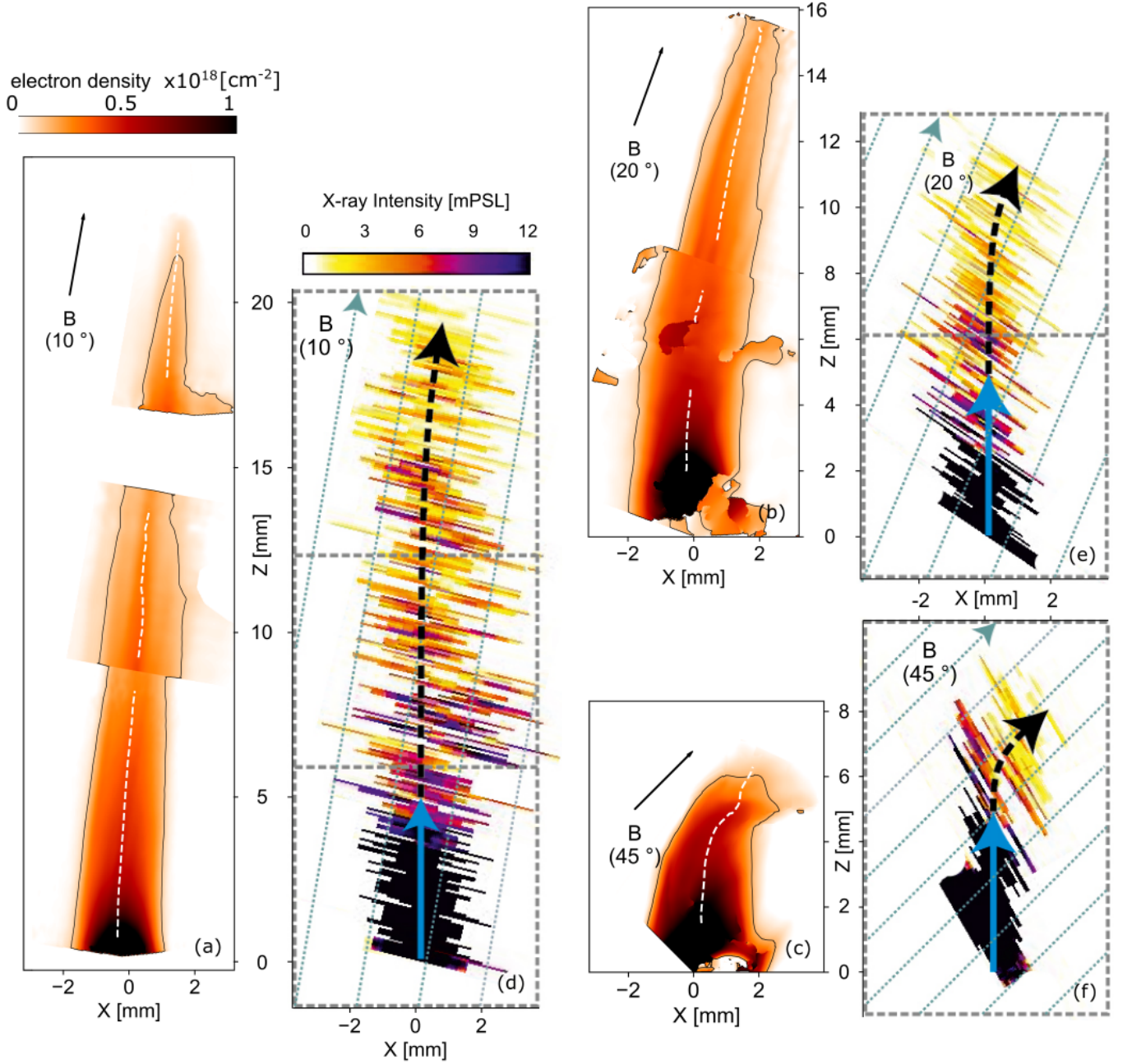


FIG. 2. **Laboratory plasma expansion observed in misaligned configurations.** (a) Laboratory electron density integrated along the probe line of sight, in a 20 T case at **36 ns**, retrieved via interferometric measurement (see Methods), with a misalignment of $\alpha = 10$ degrees between the target and the magnetic field. The target normal is along z (as illustrated by the dashed grey arrows in Fig.1A). (b) Same as (a), with $\alpha = 20$ degrees. (c) Same as (a) and (b) with $\alpha = 45$ degrees, and at **16 ns** after the laser interaction. (d, e, f) Same as (a, b, c) regarding the magnetic field angles, but as measured by X-ray spectroscopy inferred from He line emission (transition He 4p-1s on the Fluorine ion); the x-ray measurements are integrated in time (see Methods and Supplementary Note 2). In (a, b, c), the white dashed line follows the center of mass, measured from these electron density maps, assuming a constant ionisation state at a given distance from the target (the lines are interrupted when the density map is noisy or when transiting from a frame to another, in order to reconstruct the full jets – see Methods); the contour follows the $1 \times 10^{17} \text{ cm}^{-2}$ integrated density value; the black arrows indicate the initial magnetic field direction. In (d, e, f), the images are the result of a combination of different frames (shown by the dotted rectangles), in order to reconstruct the full jets (see Methods); the dashed blue lines indicate the magnetic field direction; the solid blue and dashed black arrows are here to guide the eyes on the bending of the 2D X-rays pattern. In all cases, $z = 0$ represents the target surface.

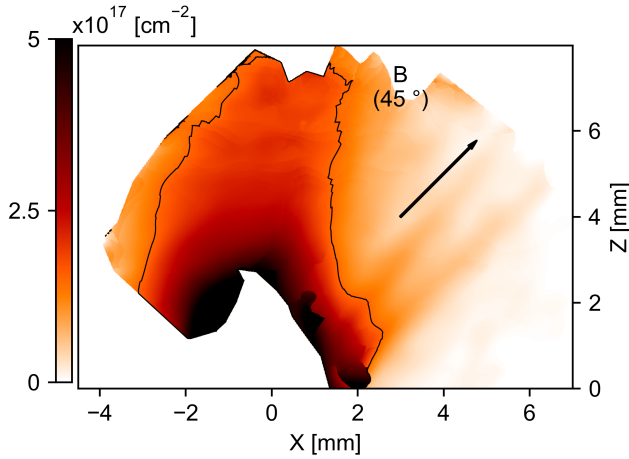


FIG. 3. **Experimental plasma expansion for large misalignment and late time.** The electron density, integrated along the probe line of sight, is shown at 45 degrees of misalignment and at **47 ns** after the start of plasma expansion. The contour follows the $1.5 \times 10^{17} \text{ cm}^{-2}$ integrated density value. The black arrow indicates the initial magnetic field direction.

distance-from-the-source region of its expansion. As illustrated in Fig.1A, by inclining the laser-irradiated target, we are able to vary the angle α of the magnetic field with respect to the main plasma flow direction. We demonstrate that (1) outflows tend to align over large scales with the direction of the magnetic field, even for an initial large misalignment of their axes, and that (2) narrow collimation (i.e. the capability for the outflow to keep a high density over large distance) is possible only for a small initial misalignment ($\lesssim 20 - 30^\circ$). The latter is due to the fact that the generation of a diamagnetic cavity is only possible for a small misalignment. That cavity results of the plasma/magnetic field interaction [23]. Having shocked edges, the cavity forms an effective magnetic nozzle, which redirects the flow into a narrow, long range and high density jet [24, 25]. These findings are corroborated by numerical three dimensional magneto-hydrodynamic (MHD) simulations performed in laboratory conditions. They are also consistent with the above-mentioned YSO's observations of the preferential alignment with the magnetic field of well collimated, long-range jets [30, 31], while in the contrary weaker and shorter jets do not display an alignment with the magnetic field. Hence, our results provide a plausible explanation for the underlying physical mechanisms explaining the varied morphologies (short vs. collimated) of jets that have been so far observed.

The perfectly plasma/magnetic field aligned case, $\alpha = 0$, represents the ideal case for the collimation of the outflow by the poloidal magnetic field. The details of the collimation mechanism through the formation

	<i>Laboratory</i>	<i>YSO</i>
B-field [G]	2×10^5	2.5×10^{-2}
Material	CF_2 (Teflon)	H
Atomic number	16.7	1.28
	early expansion	early expansion
Distance from source / Time	$100 \mu\text{m} / 1 \text{ ns}$	$10 \text{ AU} / 2 \text{ month}$
Spatial (Radial) scale [cm]	1×10^{-1}	$9 \times 10^{13} (3 \text{ AU})$
Charge state	8	2×10^{-2}
Electron Density [cm^{-3}]	2×10^{19}	3.5×10^4
Density [g cm^{-3}]	7×10^{-5}	7×10^{-18}
Te [eV]	300	3
Flow velocity [km s^{-1}]	550	250
	(100 – 1000)	(100 – 400)
β_{dyn}	133	174
Mach number	3	11
Alfvénic mach number	3	5
Magnetic Reynolds number	3×10^3	1×10^{18}
Reynolds number	5×10^4	4×10^1
Peclet number	2	6×10^4
Euler number	9	17
Alfvén number	6×10^{-4}	20×10^{-4}

TABLE I. **Comparison and scalability between the laboratory system and the one of a YSO.** The YSO density, charge state, temperature and flow velocity are extracted from Maurri et al. and Ainsworth et al. [32, 33], and correspond to the DG Tau A object and its associated HH 158 jet, just after a distance of 10 AU from the outflow source. The value for the magnetic field in the YSO outflow corresponds to that required to collimate the outflow to its observed radius (see Supplementary Note 1). The indicated velocity ranges correspond to the minimum and maximum speed within the flow; in the laboratory case it corresponds to the ballistic behavior of the expansion [34]. N.B: due to the very high Magnetic Reynolds number in both cases, and the associated very strong advection of the magnetic field lines as explained in the main text, the magnetic field is expected to be presented in the core of the outflow; hence the Reynolds and Peclet numbers do not take into account any ion or electron magnetization correction.

of an effective magnetic nozzle have been discussed in Refs. [23–25], and the reader should refer to such references to get physical insights about the collimation mechanism. As illustrated by the Fig.1B(a, b) this magnetic nozzle allows the formation of a jet collimated over long spatial and temporal ranges, in contrast with the no-external-magnetic-field expansion, where a much faster density decrease along the outflow expansion can be observed.

By increasing the angle α , we here after investigate the effect of a misalignment of the magnetic field on that collimated jet generation. The maps of Fig.2(a, b, c), for angles of 10, 20 and 45 degrees respectively, present the

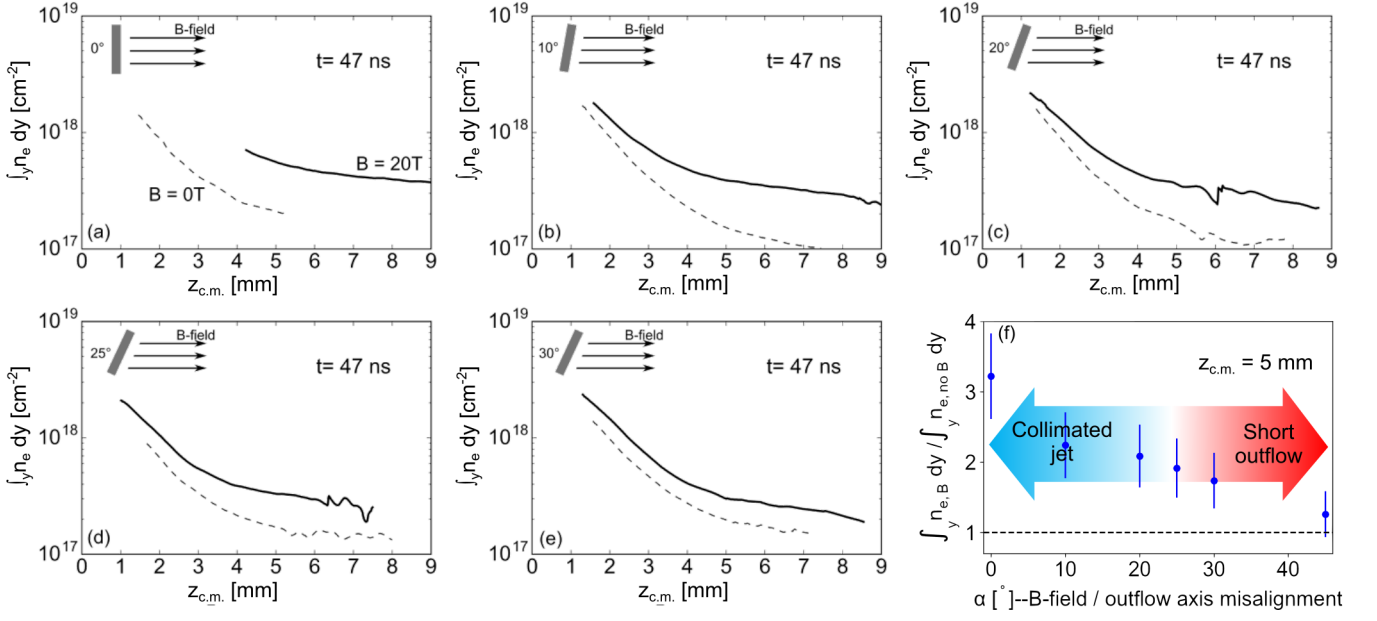


FIG. 4. **Evolution of the center of mass electron density vs. magnetic misalignment: evidence for lack of collimation.** Line of sight integrated electron density at the location of the center of mass, $\int_y n_e dy (z_{c.m.}) [cm^{-2}]$ (see text; with $z_{c.m.} = 0$ being the target surface) for different target angles (going from (a) to (e), from 0 to 30 degrees respectively) relative to the magnetic field direction, and at a time of 47 ns after the start of the plasma expansion. The solid lines show lineouts of plasma expansion in the presence of the magnetic field, while the dashed lines are lineouts without magnetic field. The profiles are voluntarily stopped for small and high z . In the first case, the high electron density is inaccessible to optical probing, or fringes quality is too poor. In the second case, the plasma flow is out of the accessible field of view. (f) Ratio $\int_y n_{e,B} dy / \int_y n_{e,no B} dy$ as a function of the magnetic field angle vs the target normal, taken at $z_{c.m.} = 5 mm$ (which is the last point at which we measure the unmagnetized outflow in all cases), and at $t = 47 ns$. The error bars calibration is detailed in the Supplementary Note 3.

electron density integrated along the probe line of sight (similarly as shown in Fig.1B(a, b) for the aligned case). In these maps, a clear curvature of the expanding plasma motion is observed and two stages are visible. Firstly, close to the target surface, the hot and dense plasma expands as expected, i.e. perpendicularly to the target surface, expelling out the magnetic field lines. Later on, farther from the target surface, the plasma flow is observed to be redirected along the magnetic field, the funnelling tending to follow the original magnetic field axis. The dashed white lines superimposed on the electron density maps help guide the eyes on that redirection as they follow the center of mass of the plasma flow. Hereafter the axis following such line will be referred to as $z_{c.m.}$. This plasma redirection is also corroborated by looking at the X-rays emission from the plasma, see Fig.2(d, e, f). Note that the X-ray data also demonstrate that, in the presence of the magnetic field, the plasmas exhibit higher temperature than that without magnetic field, irrespective of the misalignment between the flow and the magnetic field (See Supplementary Note 2 for details on the analysis). This latest experimental evidence highlight that, whatever the asymmetry of the plasma expansion is, a global heating of the plasma (through super-Alfvénic shocks [23]) occurs.

This redirection behaviour is observed to be true for small misalignments, with jets forming and being oriented along the initial magnetic field orientation up to tens of millimetres away from the target (see 10° and 20° cases at 36 ns in Fig.2(a) and (b), respectively). However, for large misalignment cases, this seems to hold only for short times (see 45° case at 16 ns in Fig.2(c)). Indeed, at later times, the outflow is unable to expand to large distances from the target and to form a narrow, cylindrically shaped, extended jet (see the 45° case at 47 ns: Fig.3). Also, there is evidence of plasma leaking, in the xz plane, far from the central axis $z_{c.m.}$. This can be seen already in the 20° case (Fig.2(b), on the right-hand side of the jet from $z = 8 mm$ to $z = 14 mm$), and it is even more obvious at the late time of the 45° case (Fig.3).

Fig.4 quantifies the decreasing collimation efficiency when increasing the misalignment between the outflow and the magnetic field. There are shown experimental longitudinal lineouts of the integrated (along y) electron density measured, at 47 ns after the laser interaction, along $z_{c.m.}$ for different magnetic field angles. In the perfectly aligned case (Fig.4(a)), the jet collimation induced by the magnetic field is obvious. This is witnessed by the rapid drop in electron density in the unmagnetised case (dashed lines) that contrasts with the flat-

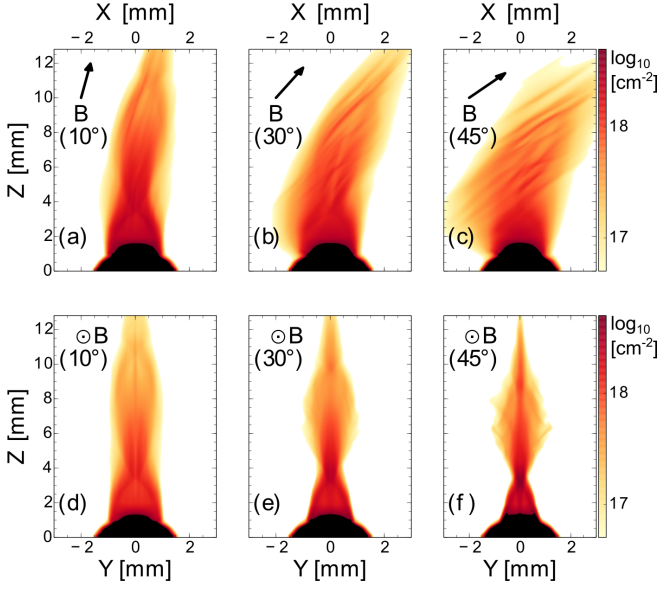


FIG. 5. **Simulated plasma expansion vs. magnetic misalignment.** 2D maps (in the xz and yz planes) of 3D MHD numerical simulations displaying the decimal logarithm of the integrated electron density along either x or y . Figures (a), (b) and (c) correspond to maps in the plane containing the magnetic field whereas figures (d), (e) and (f) correspond to maps in the plane orthogonal to the magnetic field. Thus, a, b and c correspond to the laboratory measurements shown in Fig.1B, and Figs.2 and 3. All figures correspond to a time of **18 ns** after the start of the plasma expansion. The black arrows indicate the initial magnetic field direction.

ter and higher-density profile when the 20 T magnetic field is applied (solid line). Increasing the angle α between the magnetic field and the target normal induces a decrease of the amount of plasma along the redirection axis. Fig.4(f) summarises this effect by showing the ratio $\int_y n_{e,B} dy / \int_y n_{e,no} B dy$ as a function of the magnetic field angle, taken at $z_{c.m.} = 5 \text{ mm}$. Starting from the perfectly aligned case, the ratio decreases progressively to finally tend to the value of 1. It means that in this case the expansion tends to be similar to the unmagnetised one. From this experimental evidence, we infer that asymmetric plasma expansion caused by the misaligned magnetic field disturbs the formation of the cavity responsible for jet collimation [23–25], and thus prevent the efficient forming of a dense jet.

3D MHD simulations allow us to get insight into the dynamic of the jet formation or disruption for varying outflow/magnetic field angles. In Fig.5, we show simulated maps of the integrated electron density along two lines of sight: perpendicular (a – c), i.e. as in the laboratory measurements of Fig.1B and 2, and parallel (d – f) to the magnetic field direction. The simulations are performed using the 3D resistive MHD code Gorgon (see Methods).

The simulated electron density maps of Fig.5(a – c)

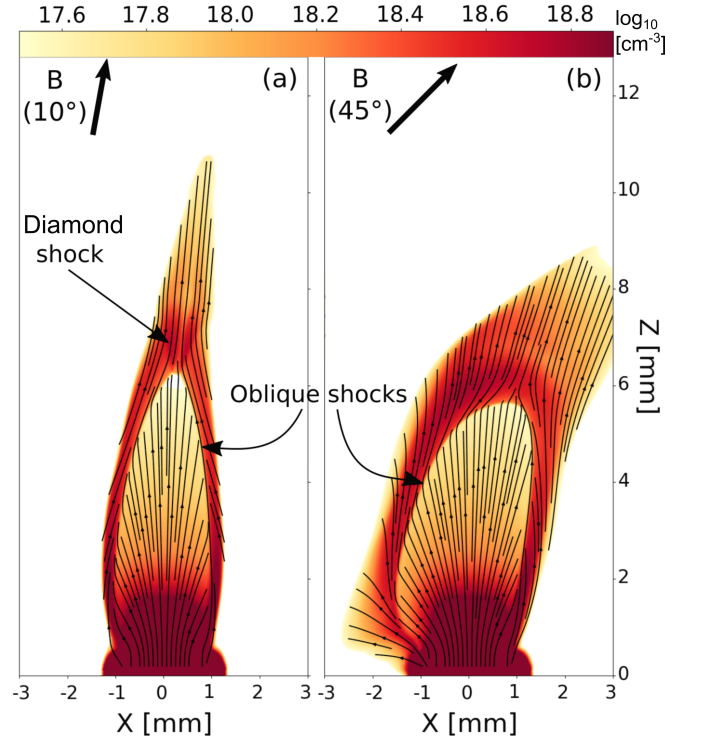


FIG. 6. **Simulation insights in the cavity formation disruption.** 2D slices of the decimal logarithm of the electron density (in the xz plane) from 3D MHD Gorgon simulations for (a) $\alpha = 10$ degrees and (b) $\alpha = 45$ degrees. Also shown are some velocity streamlines (black lines) displaying the differences in flow collimation as the angle is increased. Both images correspond to a time of **10 ns** after the start of plasma expansion.

clearly corroborate the experimental maps in terms of flow redirection, collimation and regarding flow leakage away from the central plasma structure. In addition, the perpendicular line of sight shown by Fig.5(d – f) sheds light on a strong asymmetry between the two planes (containing the magnetic field lines, xz plane, and perpendicular to the magnetic field lines, yz) for large misalignments. The strong asymmetry for the large misalignment comes as the radial plasma expansion in the x -direction is increasingly more parallel to the magnetic field lines (and so free to develop), while on the other hand the plasma expansion in the y -direction stays perpendicular to the magnetic field lines (and so hampered).

In order to understand more in detail the lack of flow collimation as the misalignment is increased, we show in Fig.6, superimposed to a x - z slice of electron density, streamlines of the velocity field for the $\alpha = 10$ degrees and $\alpha = 45$ degrees cases. The generation of oblique shocks on the cavity walls is the first significant component of the global magnetic collimation process. These are fast shocks across which the flow is efficiently redirected toward the tip of the cavity, along the cavity wall. The second important component of the collimation is

the formation of a diamond shock as a result of the converging flows (see Fig.6(a)). These secondary fast shocks redirect the converging flows which then propagate in a direction almost parallel to the original magnetic field.

As one can see in Fig.6(a), i.e. in the $\alpha = 10$ degrees case, the flow redirection is almost perfectly symmetric on each side of the cavity. At $\alpha = 45$ degrees however (Fig.6(b)) the configuration is largely asymmetric, disturbing the above mentioned schema. Indeed, while the right-side flow seems to be relatively well redirected, the left-side flow shows very little collimation as the flow encounters the magnetic field much more frontally on this side. Consequently, as the angle is increased, the flow convergence toward the cavity tip is progressively lost and the diamond shock can not effectively form. Instead, the plasma is spread in the x -direction, resulting in an expansion of the plasma perpendicularly to the magnetic field direction, pushing against the magnetic field lines more easily in the z -direction as the magnetic tension is reduced by that spread in the x -direction (See Supplementary Note 4 for more details).

DISCUSSION

Our results suggest that the large-scale collimation of the outflow in astrophysical systems depends mostly on the orientation between the ejection axis and the ambient magnetic field. The mechanism responsible for the efficient collimation of a wide-angle outflow by a poloidal component of the magnetic field [23–25] is progressively disturbed for increasing misalignment angle α between the main plasma momentum and the magnetic field. Increasing α induces intrinsic asymmetry which makes the convergence at the tip of the collimating cavity unable to be properly generated. It results in a flow not only lacking of collimation, but where also additional leakage of matter is found to develop through a Rayleigh-Taylor type of instability [35], thus decreasing even more the amount of matter distributed in a jet-like structure (see striations, witnessing Rayleigh-Taylor modes, in density maps of Figs.3 and 5 (c)).

Overall, these findings are well consistent with the ones of YSOs, [31] and [30] that show a tendency for well collimated, long range, bright jets to be aligned with the magnetic field, while oppositely, weaker and shorter jets are mainly found to be misaligned with the magnetic field. As a consequence, we claim that in a situation where a bright, long-range, and well collimated YSOs jet is observed, there is indeed good alignment between the outflow and the large scale magnetic field.

Beyond the case of YSOs, our findings also suggest that geometrical changes in the ambient magnetic field might as well explain the variations in the direction of jets of particles escaping from bow-shock PWNe (e.g. the s-shaped jet of the Lighthouse nebula [11]) and the dis-

tortions of the tail at certain distances from the pulsar (as in the case of the Mushroom nebula [14]). Usually a strong density gradient in the interstellar medium (ISM) is invoked to explain such modifications of the tail, even if most of these sources are estimated to be in underdense regions (with $\lesssim 0.1$ particles cm^{-3}). Let us consider in detail the characteristics of the mushroom nebula. It shows a bright X-ray head and a fainter elongated tail, extending for $L_{tail} \sim 7'$. Two faint asymmetric jets, called whiskers, extend from the head for $\sim 1.5'$ (the west one) and $\sim 3.5'$ (the east one) in a direction roughly orthogonal to the tail. These can be interpreted as formed by particles escaping from the bow shock and then tracing the structure of the underlying magnetic field. The condition for the tail to feel possible variations of the ISM magnetic field is the equipartition with the magnetic outer pressure. Considering an ambient magnetic field of order of $\sim 5 \mu G$, compatible with the formation of the whiskers, this condition is realized at a distance of $\sim 0.3 - 0.5 L_{tail}$, which roughly corresponds to the location at which the tail is seen to bend in the whiskers direction. Considering the structure of the ISM magnetic field to remain almost unchanged along the tail, the modification of the tail direction could thus be easily explained as the effect of the interaction of the tail plasma with the orthogonal magnetic field of the ISM, similarly to what is seen in our experiment. The distance at which the effect of the bending appears more evident in the laboratory framework, $\sim 10 mm$ with $1 mm$ being the spatial scale of the experimental system (see Fig.2 and Fig.5), is also compatible with the one estimated for the bow shock tail, of order of $10 d_0$ in the case of the Mushroom nebula, with $d_0 = \left[\dot{E} / (4\pi c \rho_{ISM} v_{PSR}^2) \right]^{1/2}$ being the spatial scale of the system (the so called stand-off distance; with \dot{E} the energy losses rate of the pulsar, or luminosity; ρ_{ISM} the interstellar medium density; v_{PSR} the pulsar velocity).

Another interesting case to discuss in the light of the present laboratory observations is the bending of highly collimated flows which has been observed in the context of extragalactic jets. Observations reveal, for instance in the case of BL Lacerte objects, that one-sided jet structures at parsec and kpc scales are strongly misaligned [36]. Prominent curvature effects are also detected in the peculiar morphology of wide-angle tail radio galaxies which cannot be accounted for by external forces (e.g. thermal pressure gradients). For these reasons, jet bending has been an active subject of debate in the extragalactic jet community for more than two decades, see e.g. [37] and the review by [38]. Although recent numerical investigations are supporting the idea of fluid instabilities-induced bending, it remains plausible that deflection could also be accounted for by the interaction with an oblique extragalactic magnetic field, as highlighted by our laboratory results. This possibility has

been explored, with the aid of three-dimensional numerical simulations [39, 40]. For weakly supersonic jets (or in equipartition), effective bending is observed by a relative angle of 45° . The effect is, however, suppressed for Mach number $\gtrsim 4$. Overall, the results obtained from these simulations (in the classical regime) favourably compare to the conclusions drawn in the present work: the bending scale depends on the relative angle between the jet and the field, the jet velocity and the plasma magnetization. Nevertheless, relativistic MHD computations indicate that relativistic jets are less affected by the field obliquity and that bending is not as strong as in the classical case.

Finally, we note that in the laboratory configuration investigated here, the fixed angle between the outflow and the large-scale magnetic field is an idealised situation. For instance, in real YSO systems, this angle can change during the lifetime of the star due to various effects, e.g. perturbations in case of binary/multiple systems, or effects of precession or nutation in the stellar rotation axis. In this frame, we could expect the produced jet, instead of being uniform, to be highly modulated and structured. Hence, our results could provide an alternative explanation to the structuring observed in jets, in the form of chains of knots and bow structures [2, 5, 41, 42], as due to variations in the angle between outflow and large-scale field. In this case, the jet structure would reflect these changes in angle and the analysis of observations of jets could provide a diagnostic to obtain information about the astrophysical system, namely the changes in the alignment of outflow and magnetic field. Similarly, observations of a s-shaped morphology of protostellar jets at parsec scales [6] could be interpreted, in the light of our results, as originating from a regular and gradual change in the direction of the ambient field, and not necessarily as due to an intrinsic precession of the jet. Indeed, if the disk axis (and the jet) is characterized by a precession but the ambient field does not change its direction, the precession should be not visible because the outflow would be always redirected in the direction of the field. However, if the jet has no precession and the ambient field changes direction, the latter would imprint a gradual change of direction of the jet on parsec scales. In short, the internal structure of YSO jets (e.g. knots, shocks) could be interpreted as the signature of changes over time in the angle between the outflow and the ambient field, when the change in the direction of the jet (as in the case of s-shaped morphology of jets) could simply be the signature of changes in the direction of the ambient field, irrespectively of the behaviour of the jet.

Acknowledgments

We thank the LULI teams for technical support, the Dresden High Magnetic Field Laboratory at Helmholtz-Zentrum Dresden-Rossendorf for the development of the pulsed power generator, B. Albertazzi and M. Nakatsut-

sumi for their prior work in laying the groundwork for the experimental platform, and P. Loiseau (CEA) for discussions. This work was supported by the European Research Council (ERC) under the European Unions Horizon 2020 research and innovation program (Grant Agreement No. 787539) and by the Ministry of Education and Science of the Russian Federation under Contract No. 14.Z50.31.0007. This work was partly done within the LABEX Plas@Par project and supported by Grant No. 11-IDEX-0004-02 from ANR (France). The reported study was funded by Russian Foundation for Basic Research, project No. 19-32-60008. O. Willi would like to acknowledge the DFG Programmes GRK 1203 and SFB/TR18. All data needed to evaluate the conclusions in the paper are present in the paper. Experimental data and simulations are respectively archived on servers at LULI and LERMA laboratories and can be consulted upon request. Part of the experimental system is covered by a patent (n° 1000183285, 2013, INPI-France). This work was granted access to the HPC resources of MesoPSL financed by the Region Ile de France. The research leading to these results is supported by Extreme Light Infrastructure Nuclear Physics (ELI-NP) Phase II, a project co-financed by the Romanian Government and European Union through the European Regional Development Fund.

METHODS

Setup of the laboratory experiment

The laboratory experiment was performed at the Elfie laser facility (LULI, Ecole Polytechnique) using a chirped laser beam of 0.6 ns duration and 40 J energy, at the wavelength of 1057 nm and focused down to a $\sim 700 \mu\text{m}$ diameter spot on a Teflon (CF_2) target. This gives a maximum intensity on target of $I_{\text{max}} = 1.6 \times 10^{13} \text{ W cm}^{-2}$.

The expanding hot Teflon plasma is coupled to an external magnetic field with large temporal (μs) and spatial (cm) scales compared to the scales of the observed laboratory plasma dynamic (100 ns, mm). The strength of the magnetic field is set to $B=20 \text{ T}$, via the coupling of a 32 kJ/16 kV capacitor bank delivering 20 kA to a Helmholtz coil, which is specifically designed to work in a vacuum chamber environment [25, 43].

The electron density is inferred using a visible optical beam within a Mach-Zehnder interferometer arrangement. The probe beam is a 100 mJ/5 ps/1057 nm (1ω) beam and crosses the interaction region perpendicularly to the plane in which the target is tilted, i.e. along the y-axis in Fig.1A. This probe pulse is frequency doubled and both frequencies (1ω and 2ω), co-propagating after the frequency doubling crystal, are split in two orthogonal

polarisations, S and P. This arrangement yields a set of four pulses (2ω -P / 2ω -S / 1ω -P / 1ω -S) that are temporally separated with delay lines by ~ 10 ns between each other. This technique allows us probing the plasma electron density at four different times for each laser shot [25]. Because of the limited field of view through the magnetic field coil (11 mm), we captured the full plasma (i.e. over several cm) evolution by moving the target, over a series of different shots, along the laser axis (z) and within the magnet assembly. This is done only over the maximum length over which the magnetic field shows little variation (we use as a criterion that B does not vary by more than 10 %) which corresponds to a total length of ≈ 25 mm within the coil. The images thus obtained are then patched in order to get the full spatial evolution of the plasma, as shown in Fig.1(a) and 2 (a, b).

The plasma X-ray emission is retrieved using a a focusing spectrometer (FSSR) with high spectral and spatial resolution (about $80 \mu\text{m}$ in this experiment) [44] (see Supplementary Note 2 for details on the analysis). This spectrometer was implemented to measure the X-ray spectra emitted by the multi-charged ions from the plasma, in the range 13 - 16 Å (800 – 950 eV) in the $m = 1$ order of reflection. The spectrometer was equipped with a spherically bent mica crystal with parameters $2d = 19.9376$ Å and curvature $R = 150$ mm. The time-integrated spectra were registered on Fujifilm Image Plate TR [45], which were placed in a cassette holder protected from optical radiation. For this, the aperture of the cassette was covered by two layers of filters made of polypropylene ($1 \mu\text{m}$) and aluminum (200 nm).

The spectrometer was aligned to record the spectrally resolved X-ray emission of the plasma with 2D spatial resolution, though with a strong astigmatism and far larger magnification factor along the jet axis than in the transverse (spectral dispersion) direction. Knowing the scaling factors in both directions, and accounting for optical distortion of the imaging system we can reconstruct a real 2D image of the jets. In order to fully reconstruct the long plasma expansion, we used different shots for which the target was located at different positions within the coil, as for the above mentioned optical measurements. Such images are shown in Fig.2(d, e, f), for various values of α .

Numerical simulations

The numerical simulations were performed using the the 3D Eulerian, radiative (optically thin approximation), resistive Magneto-Hydro-Dynamic (MHD) code GORGON [19, 46], with the possibility to rotate the angle of the uniform 20 T magnetic field with respect to the target surface plane. The initial laser deposition (up to 1 ns on a Carbon target) is modeled in axisymmetric, cylindrical geometry with the two-dimensional, three-temperature, radiative (diffusion approximation), Lagrangian, hydrodynamic code DUED [47], which is

then passed to GORGON. The purpose of this hand-off is to take advantage of the capability of the Lagrangian code to achieve very high resolution in modeling the laser-target interaction.

Scalability between the laboratory and YSO outflows

Looking at the plasma parameters (detailed in Table I), we note the good scalability of this laboratory dynamics to the astrophysical one of a YSO (e.g. the DG Tau A object and its associated HH 158 jet). We stress that we consider here the scalability to YSO outflows within the region 10 to 50 AU from the star, i.e. to outflows having already encountered a pre-collimation from about 90° to 25° full opening angle in the near zero to 10 AU region. Indeed, it can be gathered from astrophysical observations that outflows emerge with quite large initial divergence (up to 86° full opening angle [33]) from a launching region that is few AU wide in radius, centred on the star [33, 48]. Then they are progressively collimated within a distance of about 50 AU [33, 48, 49] leading, in the case where a narrow jet forms, to small divergence angles (only few degrees), which are compatible with the expected radial expansion of a supersonic collimated jet [50, 51]. We also note that this setup has already shown consistency between laboratory observations and astrophysical ones, namely a steady diamond shock at the top of the cavity corroborating steady X-ray emissions in YSO jets (as discussed in Ref. [24, 52]). The scalability is ensured by both plasmas being well described by ideal MHD. Consequently, the relevant dimensionless parameters, namely the Reynolds number ($Re = L \times v_{stream}/\nu$; L the characteristic size of the system; v_{stream} the flow velocity; ν the kinematic viscosity [53]), Peclet number ($Pe = L \times v_{stream}/\chi_{th}$; χ_{th} the thermal diffusivity [53]) and Magnetic Reynolds number ($R_m = L \times v_{stream}/\chi_m$; χ_m the magnetic diffusivity [54]) are checked to be greater than one. This ensures the momentum, heat and magnetic diffusion respectively to be negligible with respect to the advective transport of these quantities. We also verify that the Euler ($Eu = v\sqrt{\rho/P}$) and Alfvén ($Al = B/\sqrt{\mu_0 P}$) numbers are close enough between both system in order for them to evolve similarly [53, 55]. Finally, constraining the spatial scale, the velocity and the density of both systems (see Table I) we can state that 10 ns of laboratory evolution corresponds to 7.5 months of astrophysical evolution [54], and that the 2×10^5 G (20 T) magnetic field in the laboratory correspond to 29 mG for the astrophysical magnetic field, which is very consistent with the field that is required in order to generate an outflow with a radius matching the observed one (see Supplementary Note 1).

-
- [1] C.-F. Lee, H.-C. Hwang, T.-C. Ching, N. Hirano, S.-P. Lai, R. Rao, and P. T. P. Ho, *Nature Communications* **9**, 4636 (2018).
- [2] C.-F. Lee, P. T. P. Ho, Z.-Y. Li, N. Hirano, Q. Zhang, and H. Shang, *Nature Astronomy* **1**, 0152 (2017).
- [3] F. H. Shu, J. R. Najita, H. Shang, and Z.-Y. Li, in *Protostars and Planets IV*, edited by V. Mannings, A. P. Boss, and S. S. Russell (Tucson, AZ: Univ. Arizona Press, 2000) pp. 789–814.
- [4] A. Konigl and R. E. Pudritz, in *Protostars and Planets IV*, edited by V. Mannings, A. P. Boss, and S. S. Russell (Tucson, AZ: Univ. Arizona Press, 2000) p. 759.
- [5] R. Bonito, C. V. Fridlund, F. Favata, G. Micela, G. Peres, A. A. Djupvik, and R. Liseau, *Astronomy & Astrophysics* **484**, 389 (2008).
- [6] A. Frank, T. P. Ray, S. Cabrit, P. Hartigan, H. G. Arce, F. Bacciotti, J. Bally, M. Benisty, J. Eislöffel, M. Güdel, S. Lebedev, B. Nisini, and A. Raga, in *Protostars and Planets VI* (University of Arizona Press, 2014) pp. 451–474, arXiv:1402.3553v1.
- [7] P. Hartigan, J. A. Morse, B. Reipurth, S. Heathcote, and J. Bally, *The Astrophysical Journal* **559**, L157 (2001).
- [8] O. Kargaltsev and G. G. Pavlov, in *40 Years of Pulsars: Millisecond Pulsars, Magnetars and More*, American Institute of Physics Conference Series, Vol. 983, edited by C. Bassa, Z. Wang, A. Cumming, and V. M. Kaspi (2008) pp. 171–185, arXiv:0801.2602.
- [9] O. Kargaltsev, G. G. Pavlov, N. Klingler, and B. Rangelov, *Journal of Plasma Physics* **83**, 635830501 (2017), arXiv:1708.00456 [astro-ph.HE].
- [10] C. Y. Hui and W. Becker, *Astronomy & Astrophysics* **467**, 1209 (2007), astro-ph/0610505.
- [11] L. Pavan, P. Bordas, G. Pühlhofer, M. D. Filipović, A. De Horta, A. O’Brien, M. Balbo, R. Walter, E. Bozzo, C. Ferrigno, E. Crawford, and L. Stella, *Astronomy & Astrophysics* **562**, A122 (2014), arXiv:1309.6792 [astro-ph.HE].
- [12] C. Y. Hui, R. H. H. Huang, L. Trepl, N. Tetzlaff, J. Takata, E. M. H. Wu, and K. S. Cheng, *The Astrophysical Journal* **747**, 74 (2012), arXiv:1112.5816 [astro-ph.HE].
- [13] N. Klingler, O. Kargaltsev, B. Rangelov, G. G. Pavlov, B. Posselt, and C.-Y. Ng, *The Astrophysical Journal* **828**, 70 (2016), arXiv:1601.07174 [astro-ph.HE].
- [14] N. Klingler, B. Rangelov, O. Kargaltsev, G. G. Pavlov, R. W. Romani, B. Posselt, P. Slane, T. Temim, C. Y. Ng, N. Bucciantini, A. Bykov, D. A. Swartz, and R. Buehler, *The Astrophysical Journal* **833**, 253 (2016), arXiv:1610.06167 [astro-ph.HE].
- [15] B. Olmi and N. Bucciantini, *Monthly Notices of the Royal Astronomical Society* **490**, 3608 (2019), arXiv:1910.01926 [astro-ph.HE].
- [16] M. Lyutikov, *Monthly Notices of the Royal Astronomical Society* **373**, 73 (2006), arXiv:astro-ph/0604178 [astro-ph].
- [17] L. J. Dursi and C. Pfrommer, *The Astrophysical Journal* **677**, 993 (2008), arXiv:0711.0213 [astro-ph].
- [18] R. Moll, H. C. Spruit, and M. Obergaulinger, *Astronomy & Astrophysics* **492**, 621 (2008).
- [19] A. Ciardi, S. V. Lebedev, A. Frank, E. G. Blackman, J. P. Chittenden, C. J. Jennings, D. J. Ampleford, S. N. Bland, S. C. Bott, J. Rapley, G. N. Hall, F. A. Suzuki-Vidal, A. Marocchino, T. Lery, and C. Stehle, *Physics of Plasmas* **14**, 056501 (2007), arXiv:0611441 [astro-ph].
- [20] S. Matt, R. Winglee, and K.-H. Böhm, *Monthly Notices of the Royal Astronomical Society* **345**, 660 (2003).
- [21] A. Konigl, *The Astrophysical Journal* **261**, 115 (1982).
- [22] J. M. Stone and M. L. Norman, *The Astrophysical Journal* **389**, 297 (1992).
- [23] A. Ciardi, T. Vinci, J. Fuchs, B. Albertazzi, C. Riconda, H. Pépin, and O. Portugall, *Physical Review Letters* **110**, 025002 (2013), arXiv:arXiv:1212.2805v1.
- [24] B. Albertazzi, A. Ciardi, M. Nakatsutsumi, T. Vinci, J. Béard, R. Bonito, J. Billette, M. Borghesi, Z. Burkley, S. N. Chen, T. E. Cowan, T. Herrmannsdörfer, D. P. Higginson, F. Kroll, S. A. A. Pikuz, K. Naughton, L. Romagnani, C. Riconda, G. Revet, R. Riquier, H.-P. H.-P. Schlenvoigt, I. Y. Skobelev, A. Y. Faenov, A. Soloviev, M. Huarte-Espinosa, A. Frank, O. Portugall, H. Pépin, and J. Fuchs, *Science* **346**, 325 (2014).
- [25] D. P. Higginson, G. Revet, B. Khair, M. Blecher, M. Borghesi, K. Burdonov, S. N. Chen, E. Filippov, D. Khaghani, K. Naughton, S. Pikuz, O. Portugall, C. Riconda, R. Riquier, S. N. Ryazantsev, A. Soloviev, M. Starodubtsev, T. Vinci, O. Willi, A. Ciardi, and J. Fuchs, *High Energy Density Physics* **23**, 48 (2017).
- [26] J. A. Davidson, G. Novak, T. G. Matthews, B. Matthews, P. F. Goldsmith, N. Chapman, N. H. Volgenau, J. E. Vaillancourt, and M. Attard, *The Astrophysical Journal* **732**, 97 (2011).
- [27] C. L. H. Hull, R. L. Plambeck, A. D. Bolatto, G. C. Bower, J. M. Carpenter, R. M. Crutcher, J. D. Fiege, E. Franzmann, N. S. Hakobian, C. Heiles, M. Houde, A. M. Hughes, K. Jameson, W. Kwon, J. W. Lamb, L. W. Looney, B. C. Matthews, L. Mundy, T. Pillai, M. W. Pound, I. W. Stephens, J. J. Tobin, J. E. Vaillancourt, N. H. Volgenau, and M. C. H. Wright, *The Astrophysical Journal* **768**, 159 (2013).
- [28] N. L. Chapman, J. A. Davidson, P. F. Goldsmith, M. Houde, W. Kwon, Z.-Y. Li, L. W. Looney, B. Matthews, T. G. Matthews, G. Novak, R. Peng, J. E. Vaillancourt, and N. H. Volgenau, *The Astrophysical Journal* **770**, 151 (2013), arXiv:1305.2922.
- [29] C. Carrasco-González, L. F. Rodríguez, G. Anglada, J. Martí, J. M. Torrelles, and M. Osorio, *Science* **330**, 1209 (2010), arXiv:1011.6254.
- [30] K. M. Strom, S. E. Strom, S. C. Wolff, J. Morgan, and M. Wenz, *The Astrophysical Journal Supplement Series* **62**, 39 (1986).
- [31] F. Ménard and G. Duchêne, *Astronomy & Astrophysics* **425**, 973 (2004), arXiv:0407075 [astro-ph].
- [32] L. Maurri, F. Bacciotti, L. Podio, T. P. Ray, R. Mundt, U. Locatelli, and D. Coffey, *Astronomy & Astrophysics* **565**, A110 (2014).
- [33] R. E. Ainsworth, T. P. Ray, A. M. Scaife, J. S. Greaves, and R. J. Beswick, *Monthly Notices of the Royal Astronomical Society: Letters* **436**, 64 (2013).
- [34] G. Revet, B. Khair, J. Béard, R. Bonito, S. Orlando, M. Starodubtsev, A. Ciardi, and J. Fuchs, *High Energy Density Physics* **33**, 100711 (2019).
- [35] B. Khair, G. Revet, A. Ciardi, K. Burdonov, E. Filippov, J. Béard, M. Cerchez, S. N. Chen, T. Gangolf, S. S. Makarov, M. Ouillé, M. Safronova, I. Y. Skobelev, A. Soloviev, M. Starodubtsev, O. Willi, S. Pikuz, and J. Fuchs, *Physical Review Letters* **123**, 205001 (2019),

- arXiv:1910.13778.
- [36] S. Appl, H. Sol, and L. Vicente, *Astronomy & Astrophysics* **310**, 419 (1996).
 - [37] A. Mignone, P. Rossi, G. Bodo, A. Ferrari, and S. Massaglia, *Monthly Notices of the Royal Astronomical Society* **402**, 7 (2010), arXiv:0908.4523 [astro-ph.CO].
 - [38] R. Blandford, D. Meier, and A. Readhead, *Annual Review of Astron. & Astrophys.* **57**, 467 (2019), arXiv:1812.06025 [astro-ph.HE].
 - [39] S. Koide, J.-I. Sakai, K.-I. Nishikawa, and R. L. Mutel, *The Astrophysical Journal* **464**, 724 (1996).
 - [40] K.-I. Nishikawa, S. Koide, J.-i. Sakai, D. M. Christodoulou, H. Sol, and R. L. Mutel, *The Astrophysical Journal* **498**, 166 (1998).
 - [41] K.-S. Jhan and C.-F. Lee, *The Astrophysical Journal* **816**, 32 (2016).
 - [42] V. Agra-Amboage, C. Dougados, S. Cabrit, and J. Reunanen, *Astronomy & Astrophysics* **532**, A59 (2011).
 - [43] B. Albertazzi, J. Béard, A. Ciardi, T. Vinci, J. Albrecht, J. Billette, T. Burris-Mog, S. N. Chen, D. Da Silva, S. Dittrich, T. Herrmannsdörfer, B. Hirardin, F. Kroll, M. Nakatsutsumi, S. Nitsche, C. Riconda, L. Romagnani, H. P. Schlenvoigt, S. Simond, E. Veuillot, T. E. Cowan, O. Portugall, H. Pépin, and J. Fuchs, *Review of Scientific Instruments* **84**, 1 (2013).
 - [44] S. N. Ryazantsev, I. Y. Skobelev, A. Y. Faenov, T. A. Pikuz, and P. S. A. Grum-Grzhimailo, A. N., *JETP Letters* **102**, 707 (2016).
 - [45] A. L. Meadowcroft, C. D. Bentley, and E. N. Stott, *Review of Scientific Instruments* **79**, 113102 (2008).
 - [46] J. P. Chittenden, S. V. Lebedev, C. A. Jennings, S. N. Bland, and A. Ciardi, *Plasma Physics and Controlled Fusion* **46**, B457 (2004).
 - [47] S. Atzeni, A. Schiavi, F. Califano, F. Cattani, F. Cornolti, D. Del Sarto, T. V. Liseykina, A. MacChi, and F. Pegoraro, *Computer Physics Communications* **169**, 153 (2005).
 - [48] P. Hartigan, S. Edwards, and R. Pierson, *The Astrophysical Journal* **609**, 261 (2004).
 - [49] J. Woitas, T. P. Ray, F. Bacciotti, C. J. Davis, and J. Eisloffel, *The Astrophysical Journal* **580**, 336 (2002).
 - [50] C. Dougados, S. Cabrit, C. Lavalley, and F. Ménard, *Astronomy & Astrophysics* **357**, L61 (2000).
 - [51] C. J. Burrows, K. R. Stapelfeldt, A. M. Watson, J. E. Krist, G. E. Ballester, J. T. Clarke, D. Crisp, J. S. Gallagher III, R. E. Griffiths, J. Jeff Hester, J. G. Hoessel, J. A. Holtzman, J. R. Mould, P. A. Scowen, J. T. Trauger, and J. A. Westphal, *The Astrophysical Journal* **473**, 437 (2002).
 - [52] R. Bonito, S. Orlando, M. Miceli, G. Peres, G. Micela, and F. Favata, *Astrophysical Journal* **737**, 54 (2011), arXiv:1105.4081.
 - [53] D. D. Ryutov, R. P. Drake, J. Kane, E. Liang, B. A. Remington, and Wood-Vas, *The Astrophysical Journal* **518**, 821 (1999).
 - [54] D. D. Ryutov, R. P. Drake, and B. A. Remington, *The Astrophysical Journal Supplement Series* **127**, 465 (2000).
 - [55] D. D. Ryutov, B. A. Remington, H. F. Robey, and R. P. Drake, *Physics of Plasmas* **8**, 1804 (2001).

Supplementary Information: Laboratory disruption of scaled astrophysical outflows by a misaligned magnetic field

G. Revet,^{1,2,3} B. Khair,^{4,5} E. Filippov,^{6,1} C. Argiroffi,^{7,8} J. Béard,⁹ R. Bonito,⁸ M. Cerchez,¹⁰ S. N. Chen,^{1,11} T. Gangolf,^{10,2} D. P. Higginson,^{2,12} A. Mignone,¹³ B. Olmi,¹⁴ M. Ouilé,² S. N. Ryazantsev,^{6,15} I. Yu. Skobelev,^{6,16} M. I. Safronova,¹ M. Starodubtsev,¹ T. Vinci,² O. Willi,¹⁰ S. Pikuz,^{6,16} S. Orlando,⁸ A. Ciardi,⁴ and J. Fuchs^{1,2}

¹*Institute of Applied Physics, 46 Ulyanov Street, 603950 Nizhny Novgorod, Russia*

²*LULI, CNRS, CEA, Sorbonne Université, École Polytechnique, Institut Polytechnique de Paris, F-91128 Palaiseau, France*

³*Centre Laser Intenses et Applications, Université de Bordeaux-CNRS-CEA, UMR 5107, 33405 Talence, France*

⁴*Sorbonne Université, Observatoire de Paris, PSL Research University, LERMA, CNRS UMR 8112, F-75005, Paris, France*

⁵*Flash Center for Computational Science, University of Chicago, 5640 S. Ellis Avenue, Chicago, IL 60637, USA*

⁶*Joint Institute for High Temperatures, RAS, 125412, Moscow, Russia*

⁷*Dipartimento di Fisica e Chimica, Università di Palermo, Palermo, Italy*

⁸*INAF-Osservatorio Astronomico di Palermo, Palermo, Italy*

⁹*LNCMI, UPR 3228, CNRS-UGA-UPS-INSA, 31400 Toulouse, France*

¹⁰*Institut für Laser und Plasmaphysik, Heinrich Heine Universität Düsseldorf, D-40225 Düsseldorf, Germany*

¹¹*ELI-NP, "Horia Hulubei" National Institute for Physics and Nuclear Engineering, 30 Reactorului Street, RO-077125, Bucharest-Magurele, Romania*

¹²*Lawrence Livermore National Laboratory, Livermore, California 94550, USA*

¹³*Dip. di Fisica, Università di Torino via Pietro Giuria 1 (10125) Torino, Italy*

¹⁴*INAF-Osservatorio Astrofisico di Arcetri, Firenze, Italy*

¹⁵*M. V. Lomonosov Moscow State University, Moscow 119991, Russia*

¹⁶*National Research Nuclear University 'MEPhI', 115409 Moscow, Russia*

SUPPLEMENTARY NOTE 1: COLLIMATION RADIUS

By equalizing the ram pressure of the expanding ejecta ($P_{out} = \dot{M}_{out} \times v_{out}/S$) and the magnetic pressure ($P_{mag} = B^2/8\pi$), it is possible to show that the collimation radius (i.e. the cavity border location), i.e. where $P_{out} = P_{mag}$, is $R_c = (2 \times \dot{M}_{out} \times v_{out})^{1/2} B^{-1}$ [1]; where B is the magnetic field, $\dot{M}_{out} = \rho \times v_{out} \times S$ the ejected mass rate passing through the sphere surface $S = 4\pi R^2$ and v_{out} the speed of the ejecta.

This leads in practice, within the distance-from-the-source region $10 < z < 50$ AU, for a flow velocity of 400 km s^{-1} [2] and an ejected mass rate of $10^8 M_\odot \text{ yr}^{-1}$ [2, 3] to a magnetic field of $B = 24 \text{ mG}$ necessary for stopping the outflow within the observed collimation radius of $R_c \sim 15 \text{ AU}$ [3].

SUPPLEMENTARY NOTE 2: X-RAY SPECTROSCOPY MEASUREMENT

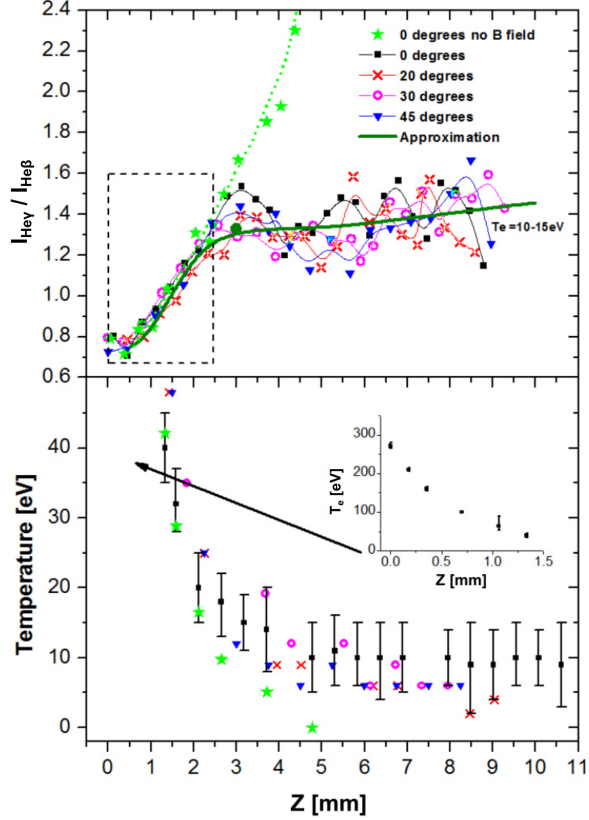
Complementarily to the optically-measured electron density maps shown in Fig.1 to 3 of the main text, the electron temperature and dynamics of jet expansion were also studied by means of X-ray spectroscopy, looking at the He-like and H-like Fluorine ions.

The 2D X-ray maps presented in Fig.2(d, e, f) of the main text support the optical interferometry data, in particular as they show the same phenomenon: the plasma initially expands normal to the source target, but later

on bends, finally following the magnetic field lines direction. They also show that the dense part of the plasma flow, dense enough to yield detectable X-ray emission, is much shortened when α increases.

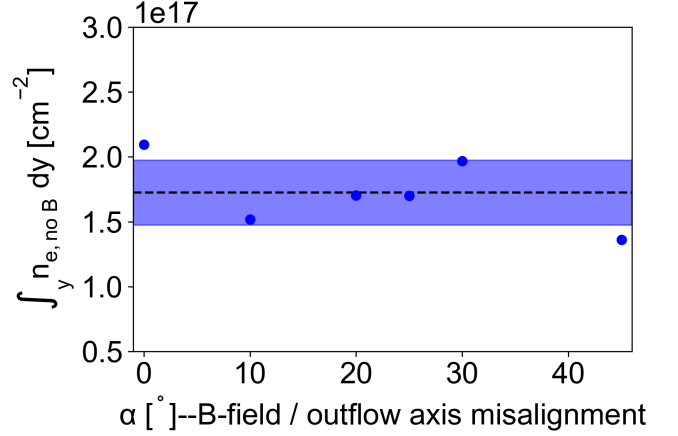
In Fig.2(d, e, f), only the images retrieved from the F He 4p-1s line emission are presented, however we can state that other observed spectral lines reveal a quite similar behavior. We note that the overall plasma evolution features and distances of sustained propagation, as retrieved from the interferometry diagnostic and the X-ray images, when the jet is observed to be deflected by the magnetic field, are similar. Thus, both diagnostics concur to demonstrate that the initial plasma expansion occurs normal to the target surface and is identical to the case with no B field. Also, both diagnostics observe that the final jet propagation direction is imposed by the B field orientation and not by the initial outflow expansion axis.

The electron temperature along the plasma jet axis was determined by analyzing the relative intensities of He γ to He β spectral lines. The method [4] is based on the quasi-steady model of expanding plasmas which also takes into account a recombining plasma model with a frozen ion charge. The results are shown in Supplementary Figure 1. While the electron temperature T_e on the laser irradiated target surface is about 300 eV, it drops down to 20 eV at a 2.5 mm distance from the target surface. Over this range, the lines intensity ratios and, correspondingly, the temperatures are almost the same regardless of the direction of the applied external mag-



Supplementary Figure 1. (top) Fluorine $\text{He}\gamma$ to $\text{He}\beta$ lines intensity ratio measured along the jet axis for different orientations of the magnetic field, i.e. 0, 20, 30 and 45 degrees, with respect to the plane of the target and also in the case when no magnetic field is applied. The dashed rectangle delimits the range where the plasma ram pressure dominates the external B field pressure, and where the line ratios are observed to be equal for all cases, as expected. (bottom) Corresponding time-integrated electron temperature of the jet plasma and as revealed by means of our recombining plasma model method. The inset corresponds to the region near the target surface where the temperature is above 50 eV.

netic field, or even of the existence of the latest. In the initial plasma expansion zone, this can be understood as the ram pressure strongly prevails over the magnetic field pressure. Beyond this initial expansion, the presence of the magnetic field allows in a case of perfectly aligned field and plasma expansion to keep the temperature of the formed jet almost constant in the range of 10 ± 5 eV at least for 8 mm long, consistently with our previous observations [4–6]. This is significantly different from the case without magnetic field, in which the temperature of the jet rapidly drops below 5 eV, as the density decreases to values smaller than 10^{18} cm^{-3} , i.e. beyond a distance of 4 mm from the target (see Supplementary Figure 1). In the presence of the magnetic field, our measurements show that similar temperatures are recorded when we



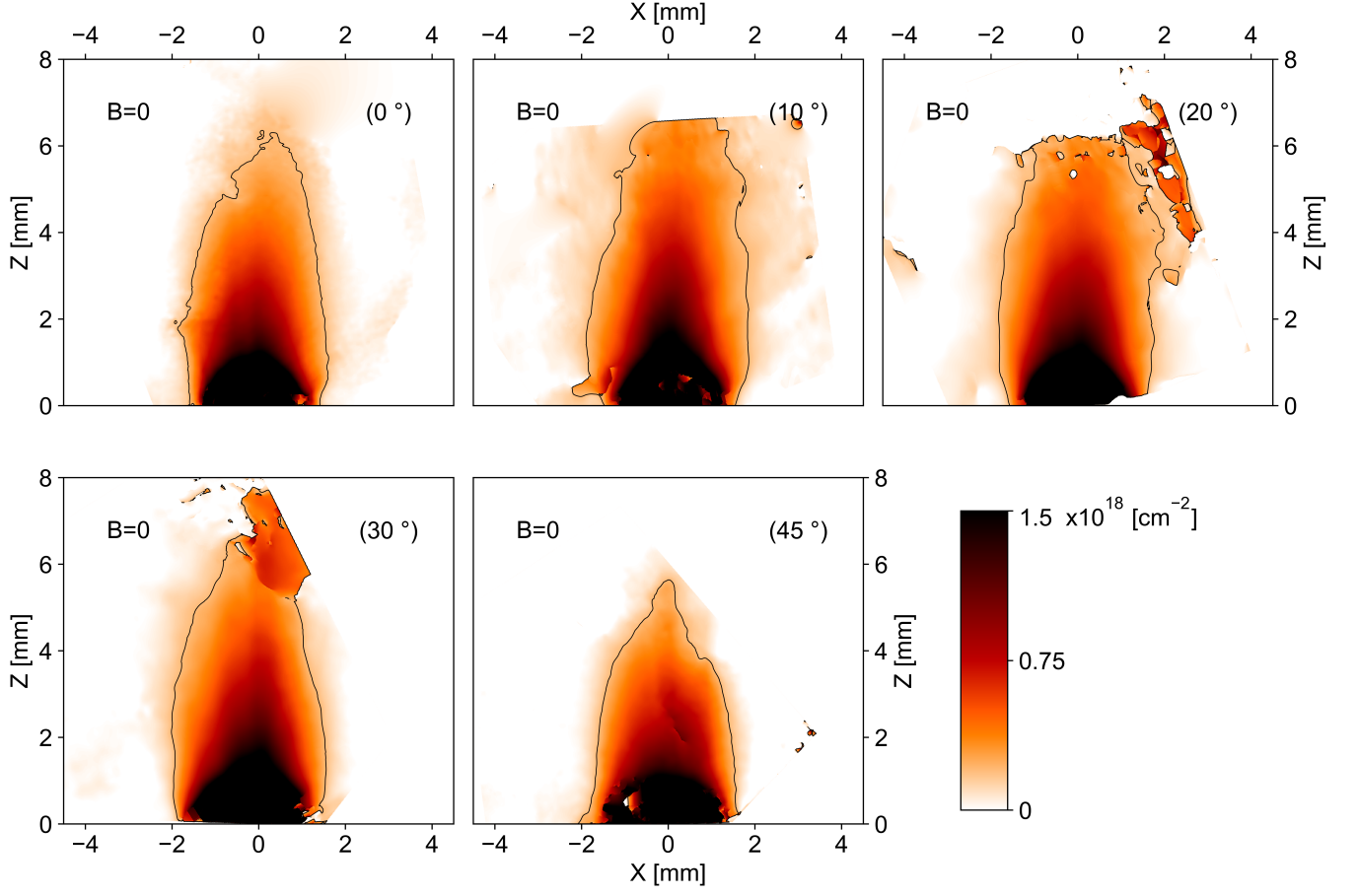
Supplementary Figure 2. Fluctuation of the integrated plasma density at the location $z_{c.m.} = 5 \text{ mm}$ for different target angles, at 16 ns after the laser interaction. The blue rectangle displays the standard deviation of the set of points measured for different angles with respect to the constant defined as the average of the points (materialized by the dashed horizontal line).

vary the direction of the applied magnetic field. However, we have to note that our method is not sensitive enough in the range of 0 to 10 eV temperatures, due to very low signal to noise ratio in the spectral line intensity data. Hence, although we can see that the plasma certainly stays hotter when the magnetic field is applied than without it, we can not determine with high precision significant temperature differences in the cases where the magnetic field orientation is modified.

SUPPLEMENTARY NOTE 3: STABILITY OF THE LASER-SOLID INTERACTION AND PLASMA EXPANSION REGARDING THE TARGET ORIENTATION WITH RESPECT TO THE HIGH-POWER LASER

In order to examine the effect of the target angle on the plasma expansion, we look at the variation of the plasma density at the location $z_{c.m.} = 5 \text{ mm}$ for cases without any magnetic field applied and for different target angles (and so different laser shots). This is summarized in Supplementary Figure 2. As can be observed, fluctuations around the mean value indicated by the dashed line are moderate and no increasing or decreasing trend is observed in the plasma density when varying the target angle. Thus, a fluctuation around a constant value seems to adequately describe the density at a given distance in the unmagnetized case. This fluctuation is attributed to the laser energy shot-to-shot fluctuations.

We note here that the standard deviation over the con-



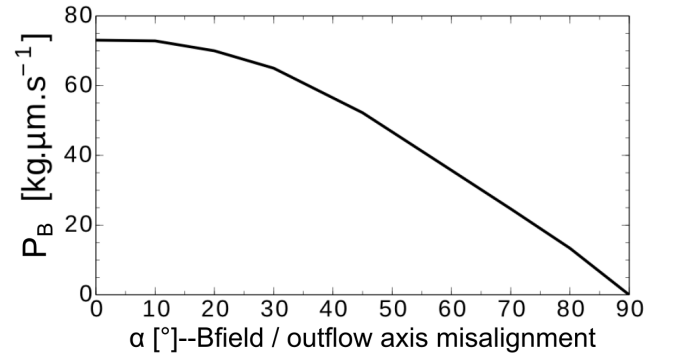
Supplementary Figure 3. Experimental integrated density of plasma expansion recorded for different target angles, at **16 ns** after the laser interaction in the absence of the external magnetic field. The black lines follow the contour of the integrated electron density of $2 \times 10^{17} \text{ cm}^{-2}$.

stant value found here is taken as the typical uncertainty on the plasma density measurements. Then, the error bars of Fig.4(f) of the main text are calculated with this error for both, the density with and without magnetic field, at $z_{c.m.} = 5 \text{ mm}$.

Also, the complete 2D integrated electron density maps at 28 ns, for different angles, are displayed in Supplementary Figure 3.

SUPPLEMENTARY NOTE 4: ADDITIONAL DISCUSSION FROM THE GORGON 3D-MHD SIMULATIONS

As illustrated by the Fig.6 of the main text, in the case of a large angle between the plasma flow and the magnetic field, the two components (cavity wall oblique shocks + cavity tip diamond shock) of the magnetic nozzle are unable to efficiently force the flow to align with the initial magnetic field direction over large scales. The plasma flow, at the tip of the cavity, is spread instead along the x -direction instead. This generates a plasma



Supplementary Figure 4. Spatially and temporally averaged momentum of the plasma along the direction of the magnetic field as a function of the misalignment angle α , retrieved from the simulations shown in Fig.5 of the main text. The plasma momentum is averaged spatially over the full simulation domain ($6 \times 6 \times 13 \text{ mm}$) and temporally over the full simulation duration (100 ns).

front, extended in the x -direction, which then actively reduces the bending of the magnetic field lines. Such a bending reduction, finally reduces drastically the ability of the magnetic forces to act against the plasma propagation. The plasma sheet, still quite hot and conductive, then pushes in the z -direction the magnetic field lines, frozen-in the plasma, in a much more favourable planar way. This has to be opposed to the initial plasma redirection at the cavity borders: the advection of the magnetic field is limited here, as a strong bending of the lines is observed, and the plasma is slowed down much more easily. Finally, the plasma sheet, while growing in size in the x -direction (reducing further the magnetic field lines bending), progresses in the z -direction ; as also attested by the declining trend of the plasma momentum aligned with the magnetic field lines.

Another observable, bringing to light the lack of collimation of the outflow with increasing the misalignment, is the momentum parallel to the local magnetic field, $P_{\parallel B}$, resulting from the whole process. Supplementary Figure 4 displays the evolution of such momentum with the misalignment. One can observe that $P_{\parallel B}$ stays similar between the perfectly aligned (0°) case (where the plasma flow is redirected along the magnetic field lines at best) and the 10° case, pointing out the efficient redirection of the plasma flow for such small misalignment. After this point however, $P_{\parallel B}$ starts to decrease and progressively reaches zero at an extreme misalignment of $\alpha = 90^\circ$: the whole plasma then propagates perpendic-

ularly to the magnetic field lines, advecting them in a perfectly planar way.

-
- [1] S. Matt, R. Winglee, and K.-H. Böhm, *Monthly Notices of the Royal Astronomical Society* **345**, 660 (2003).
 - [2] L. Maurri, F. Bacciotti, L. Podio, T. P. Ray, R. Mundt, U. Locatelli, and D. Coffey, *Astronomy & Astrophysics* **565**, A110 (2014).
 - [3] R. E. Ainsworth, T. P. Ray, A. M. Scaife, J. S. Greaves, and R. J. Beswick, *Monthly Notices of the Royal Astronomical Society: Letters* **436**, 64 (2013).
 - [4] S. N. Ryazantsev, I. Y. Skobelev, A. Y. Faenov, T. A. Pikuz, and P. S. A. Grum-Grzhimailo, A. N., *JETP Letters* **102**, 707 (2016).
 - [5] B. Albertazzi, A. Ciardi, M. Nakatsutsumi, T. Vinci, J. Béard, R. Bonito, J. Billette, M. Borghesi, Z. Burkley, S. N. Chen, T. E. Cowan, T. Herrmannsdörfer, D. P. Higginson, F. Kroll, S. A. A. Pikuz, K. Naughton, L. Romagnani, C. Riconda, G. Revet, R. Riquier, H.-P. H.-P. Schlenvoigt, I. Y. Skobelev, A. Y. Faenov, A. Soloviev, M. Huarte-Espinosa, A. Frank, O. Portugall, H. Pépin, and J. Fuchs, *Science* **346**, 325 (2014).
 - [6] D. P. Higginson, G. Revet, B. Khiar, M. Blecher, M. Borghesi, K. Burdonov, S. N. Chen, E. Filippov, D. Khaghani, K. Naughton, S. Pikuz, O. Portugall, C. Riconda, R. Riquier, S. N. Ryazantsev, A. Soloviev, M. Star-dubtsev, T. Vinci, O. Willi, A. Ciardi, and J. Fuchs, *High Energy Density Physics* **23**, 48 (2017).